Urban Climate 52 (2023) 101675

Contents lists available at ScienceDirect

Urban Climate

journal homepage: www.elsevier.com/locate/uclim

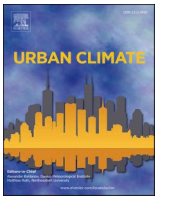

Human heat health index (H3I) for holistic assessment of heat hazard and mitigation strategies beyond urban heat islands

Harsh G. Kamath [a,*], Alberto Martilli [b], Manmeet Singh [a], Trevor Brooks [a], Kevin Lanza [c], R. Patrick Bixler [d], Marc Coudert [e], Zong-Liang Yang [a], Dev Niyogi [a,f,*]

[a] The University of Texas at Austin, Jackson School of Geosciences, 23 San Jacinto Blvd, Austin, TX 78712, USA
[b] CIEMAT, Av. Complutense, 40, 28040 Madrid, Spain
[c] The University of Texas Health Science Center at Houston, School of Public Health in Austin, 1616 Guadalupe St, Suite 6.300, Austin, TX 78701, USA
[d] University of Texas at Austin, LBJ School of Public Affairs, 2315 Red River St, Austin, TX 78712, USA
[e] City of Austin, Office of Resilience, 301 W 2nd St, Austin, TX 78701, USA
[f] University of Texas at Austin, Cockrell School of Engineering, 301 E Dean Keeton St, Austin, TX 78712, USA

ARTICLE INFO

Keywords:
Heat hazard
SOLWEIG
SoVI
SUEWS
Urban heat island
UTCI

ABSTRACT

Certain urban neighborhoods are more susceptible to heat than others, primarily because of the unequal distribution of imperviousness, building and vegetation morphology, social vulnerability, and anthropogenic heat release. Here, we demonstrate that using the surface urban heat island intensity obtained through remote sensing approaches to evaluate urban heat vulnerability (UHV) can be misleading due to the interannual and seasonal variability of rural land surface temperature (LST). We present the disparity in the heat vulnerability index (HVI) when LST and air temperature are used as hazards and show that the LST-based approach overestimates the HVI during daytime. Thus, we contend that while HVI may be appropriate for comparing the *relative* UHV of different neighborhoods, it should not be used to assess *absolute* daytime heat vulnerability. To address this limitation, we propose a new metric: human heat health index (H3I) that can be utilized to (i) assess and compare heat hazard in different neighborhoods and (ii) evaluate the effectiveness of environmental interventions for heat mitigation. H3I was applied to demonstrate the reduction in heat hazard due to 3-D urban structures using street-level modeling in Austin, Texas. Our findings emphasize the need for combining 3-D urban data, modeling, and community feedbacks efforts to assess daytime UHV for prioritizing the implementation of heat mitigation strategies.

1. Introduction

Urban areas are subject to various local stressors that are compounded by heat stress. In the United States alone, extreme heat was the leading cause of weather-related deaths, especially in urban areas for the year 2021 (NOAA, 2021). As a result, efforts are underway to develop heat mitigation strategies at the neighborhood as well as street scales, and for improving city-scale weather

* Corresponding authors at: The University of Texas at Austin, Jackson School of Geosciences, 23 San Jacinto Blvd, Austin, TX 78712, USA.
E-mail addresses: kamath.harsh@utexas.edu (H.G. Kamath), alberto.martilli@ciemat.es (A. Martilli), manmeet.singh@utexas.edu (M. Singh), tbrooks4343@utexas.edu (T. Brooks), kevin.l.lanza@uth.tmc.edu (K. Lanza), rpbixler@utexas.edu (R.P. Bixler), marc.coudert@austintexas.gov (M. Coudert), liang@jsg.utexas.edu (Z.-L. Yang), dev.niyogi@jsg.utexas.edu (D. Niyogi).

https://doi.org/10.1016/j.uclim.2023.101675
Received 5 August 2023; Accepted 7 September 2023
Available online 25 September 2023

predictions to combat the health and socioeconomic impacts of heat. Urban heat islands (UHI) cause thermal discomfort and increase the energy demand for cooling because the land surface temperature (LST) and near-surface 2-m air temperature (T2M) in cities are greater than those in the surrounding rural regions, especially at night. UHI intensity is often characterized by the differences in LST and/or T2M between urban and neighboring rural areas (Chow and Roth, 2006; Peng et al., 2012). Therefore, the UHI intensity is influenced not only by urban characteristics such as the thermal properties of building materials, anthropogenic heat emissions, reduced evapotranspiration, reduced air circulation due to built-up land, and longwave emissions from the surrounding warm environment (Oke, 1982), but also by rural characteristics such as soil moisture deficit, which modulate the rural diurnal temperature range (Niyogi et al., 2006). Since the UHI effect is predominantly a nighttime phenomenon and heat stress is greatest during the day, the UHI intensity is not a suitable measure of daytime heat hazard in urban settings. Therefore, regardless of the temperature in rural areas, absolute urban temperatures must be utilized to assess heat hazard (Martilli et al., 2020). Hence, it is apparent that a better approach than using UHI intensity is needed to highlight the daytime urban heat hazard. Nonetheless, UHI intensity can help address the negative impact of nocturnal temperatures on humans during prolonged heatwave episodes, as nighttime elevated temperatures do not allow the body to recover from daytime heat stress (Laaidi et al., 2012).

Urban areas have a higher population concentration relative to rural areas and heat affects urban communities disproportionately, mainly because of the following:

1. *The non-uniform distribution of urban heat (hazard)*: This led to the development of local climate zones (LCZ) as an extended list of land use classifications that consider physical characteristics, such as the sky view factor (SVF), which are relatively homogeneous over an urban block (Stewart and Oke, 2012). Using a supervised classification algorithm and training labels from local city experts or Google Earth photos, LCZ maps for a city can be generated from Landsat-8 data (Ching et al., 2018; Fung et al., 2022). This approach allows for reporting of typical LST and/or T2M over an urban block.
2. *Sensitivity to heat*: Urban heat vulnerability cannot be determined solely by LST and/or T2M because certain social groups may be more sensitive to heat stress than others, while some may be more adaptable. Therefore, assessing urban heat vulnerability requires considering both the hazard and social vulnerability. A popular approach to quantifying population vulnerablity that accounts for sensitivity and adaptive capacity is the social vulnerability index (SoVI) (Cutter et al., 2003).

To address the heat hazard, mitigation strategies such as cool roofs and pavements are often designed. Also, community strategies like public cooling centers are aimed to reduce SoVI by increasing the adaptive capacity. Krayenhoff and Voogt (2010) suggested that heat mitigation strategies should focus on reducing the negative consequences of heat rather than mitigating the UHI effect.

We contend that a heat hazard assessment should account for full urban geometry and its thermal effects through shortwave and longwave radiation, winds, and humidity. Despite the existence of measures like the universal thermal climate index (UTCI) (Jendritzky et al., 2012) to address this, city-scale UTCI simulations are rare due to the limited availability of urban data and the spatial scale of simulations. Alternatively, the US national weather service (NWS) uses the heat index (HI) (Rothfusz and Headquarters, 1990), which combines T2M and relative humidity (RH) to account for reduced heat loss from perspiration when RH is high, thereby increasing thermal stress. Thus, HI can be used for heat hazard assessment when the air in an urban area is not supersaturated.

The main goal of this study is to draw attention to and build on the limitations of using urban LST and/or T2M alone for assessing heat health risks and to propose a new metric for better urban heat vulnerability assessment and planning of heat mitigation strategies. We also emphasize the importance of community engagement in the planning of heat mitigation strategies and compare community perceptions of heat with observed T2M. In this work, the city of Austin Texas, was used as a representative sprawling city due to its

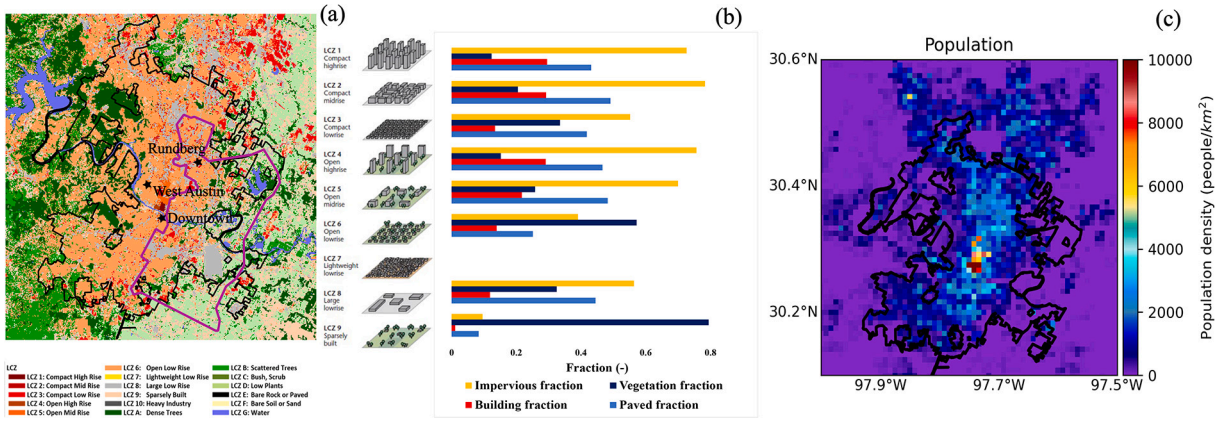

Fig. 1. (a) Austin local climate zones (LCZ) classification. Black and purple polygons show Austin city limit and region where vehicle traverse temperature data was collected, respectively. Neighborhoods in different LCZs that were chosen for model-based study are also shown. (b) fraction of vegetation (λ_v), building (λ_b) and impervious (λ_i) area within each LCZ. (c) NASA's socioeconomic data and application center (SEDAC) population density for the year 2020. (For interpretation of the references to color in this figure legend, the reader is referred to the web version of this article.)

ongoing activities and plans for implementing heat mitigation strategies that required high-resolution information for vulnerable neighborhoods.

2. Study area

The city of Austin Texas, United States, spans approximately 772 km^2 and has nearly one million residents (US Census Bureau, 2022). With the effects of global warming and urbanization, the city has seen an increase in the number of days with high temperatures exceeding the 95th percentile of climatological values. This has led to severe heat stress in neighborhoods that are vulnerable, often populated by low-income Hispanic communities (Lanza et al., 2023)(Bixler et al., 2022). According to the Köppen-Geiger climate classification (Beck et al., 2018), which takes into account both yearly and seasonal variations in temperature and precipitation, Austin is located within the humid sub-tropical climatic zone. While July and August are often the warmest months of the year, the city sees two rainfall maxima before and after the summer season.

Cities create microclimates due to their diverse land cover. It is therefore important to have an understanding of the spatial characteristics of a city using LCZs to make an initial assessment of heat vulnerability. For example, an area with intense urban development but with well-irrigated parks and vegetation may have a lower temperature on average compared to a neighborhood surrounded completely by impervious surfaces. In this study, LCZ data for the year 2019 shown in Fig. 1a was processed at 100-m spatial resolution using Landsat-8 sensor data, impervious area, and building data as inputs to a random forest model that was trained to predict LCZs using labels from Google Earth (Fung et al., 2022). The combined proportion of buildings and paved areas is denoted by the impervious fraction (λ_i), while the vegetation fraction combines trees and grass and is represented by λ_v. These fractions were obtained from a 1-m resolution land cover dataset created by fusing the 2020 European Space Agency (ESA) world-cover data with building footprints and road network from the city. The land cover dataset has 7 categories: buildings, paved surfaces, deciduous trees, evergreen trees, grass, soil, and water. This dataset is further used for modeling as discussed ahead.

Austin has predominantly open-low (LCZ_6) land cover. Fig. 1b shows a decrease in λ_i and an increase in λ_v as we go from urban regions to more natural land types. These fractions affect T2M through the surface energy balance (SEB) as they dictate the partitioning of turbulent heat fluxes. Fig. 1c displays the population density for the year 2020 using data from the NASA SEDAC (2018) gridded dataset. Population density is strongly correlated with energy consumption and therefore the release of anthropogenic heat (AH). AH is an important component of the urban surface energy balance that influences temperature.

3. Datasets and models

When using observational T2M datasets, there is a trade-off between spatial and temporal coverage. Weather stations provide high temporal resolution but only represent a small area of urban microclimate rather than the entire city. In contrast, vehicle traverse T2M observations provide greater spatial coverage but may lack temporal resolution. Similarly, when using remotely sensed LST, sensors that offer high spatial resolution typically provide data in a return cycle of ~4–5 days. Therefore, a combination of different datasets is necessary for mapping the urban thermal environment.

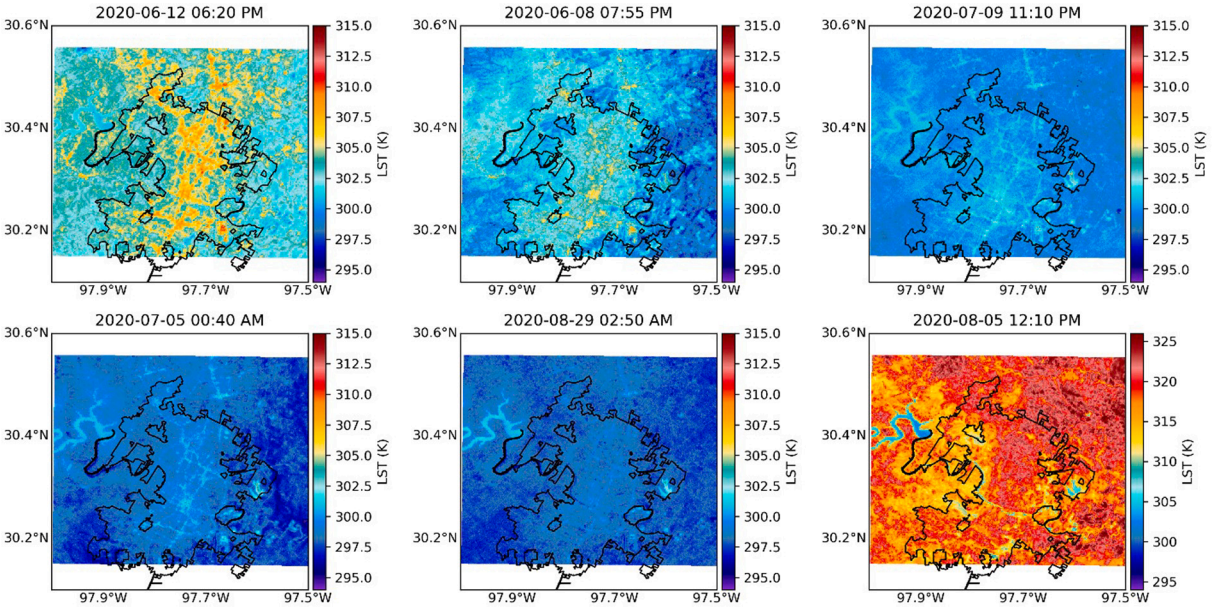

Fig. 2. ECOSTRESS land surface temperature (LST) for summer 2020 at ~70-m spatial resolution over Austin. All times indicated are local.

3.1. Remote sensing

This study used Moderate Resolution Imaging Spectroradiometer (MODIS)-Aqua to understand the interannual variability of LST in urban and surrounding rural areas in Austin. MODIS-Aqua is a sun-synchronous imager with 36 spectral bands in various wavelengths ranging from visible to thermal infrared, and it has a spatial resolution of ~1 km. Data is acquired daily during the daytime (1.30 PM local) and nighttime (1.30 AM local), and the improved MYD21 LST product was used in this study. Although MODIS has a relatively coarse spatial resolution for neighborhood scale analysis, it has LST records going back to the year 2002.

The ECO2LSTE product from the ECOsystem Spaceborne Thermal Radiometer Experiment on Space Station (ECOSTRESS) was used to analyze LST at the scale of a city block. ECOSTRESS is a radiometer that is installed on the International Space Station and operates in a non-sun-synchronous orbit with a repetition cycle of approximately 4–5 days. Data from ECOSTRESS is accessible starting in 2019, and its spatial resolution is ~70 m.`

It is important to note that remotely sensed LST data do not represent the temperature of the entire urban surface (Voogt and Oke, 1997). As a result, the LST values obtained through remote sensing may be higher during the day and lower during the night compared to the temperature of the complete urban surface. This is because roofs tend to be hotter during the day and cooler during the night due to their thermal properties and SVF (Oke et al., 2017). Further, there is uncertainty in LST estimation at large off-nadir viewing angles. In this study, however, we have not filtered data based on viewing angles. The LST retrievals might also be affected by the local weather prior to data collection. For example, cloudy conditions before image acquisition may result in lower LST estimations due to the cloud shadow effect. Lastly, ECOSTRESS geolocation accuracy may suffer under cloudy conditions, which can impact street scale analysis. These factors play a role while studying the surface UHI intensity (SUHII).

Fig. 2 presents the LST for summer of 2020, considering only cloud-free images over our extended study area to avoid the cloud shadow effect. The Figure illustrates how the LST decreases after sunset. Note that we cannot create a diurnal profile of LST from the subplots in Fig. 2 because they are from separate days.

3.2. Mobile traverse

On a clear and calm day (August 7, 2020), a urban heat mapping campaign was conducted in Austin, with 17 volunteers participating in vehicle traverse heat mapping. Fig. 1 shows that the campaign concentrated on the eastern part of the city since it included a larger proportion of low-income groups, and less tree cover, making its residents more at risk from the heat (Lanza et al., 2023). Vehicle traversal measurements were taken in the early morning (between 6 and 7 AM), afternoon (between 3 and 4 PM), and evening (between 7 and 8 PM) along the pathways depicted in Fig. S1 in the supplementary material. For the analysis in this paper, we used spatially interpolated T2M data according to Shandas et al. (2019). The interpolated air temperature is shown in Fig. 3. However, it should be noted that spatial interpolation may introduce some bias in the T2M analysis.

3.3. Models

In Austin, where there is a dearth of ground-based weather stations in various LCZs, we employed the surface urban energy and water balancing scheme (SUEWS) (Sun and Grimmond, 2019) to estimate T2M and RH at a local scale (400 × 400-m grid box). The SUEWS model has been validated in prior studies (Järvi et al., 2011; Ward et al., 2016). We used ERA-5 hourly reanalysis data for T2M, wind speed, and humidity in the inertial sub-layer for forcing SUEWS following Tang et al. (2021). Due to the low spatial resolution of ERA-5 (0.25° × 0.25°), forcing for all the neighborhoods simulated were contained within a single ERA-5 grid cell. To calculate the urban canopy parameters for SUEWS, we rasterized building and vegetation layers from the United States Geological Survey 3DEP LiDAR point cloud data. Additionally, we used the 7-class land use data as described in section 2. The SUEWS physics parametrizations used were the same as Tang et al. (2021).

The solar and longwave environmental irradiance geometry (SOLWEIG) model was used to simulate shadows, mean radiant

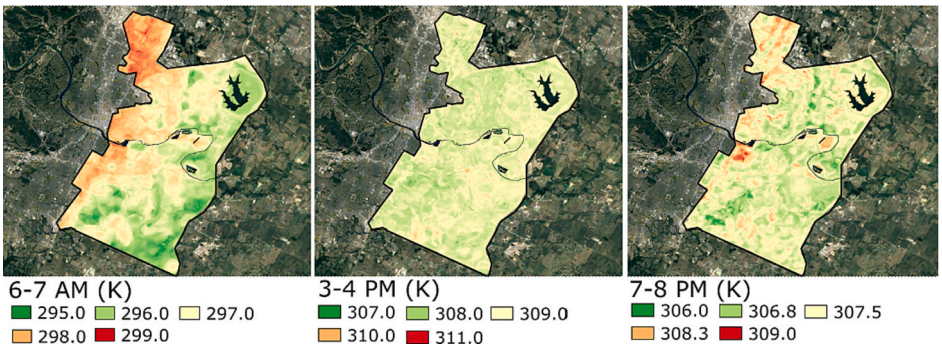

Fig. 3. Interpolated vehicle traversed 2-meter air temperature (T2M) for 7th August 2020 (summer season, June - August). Note the range of the temperature scale is different for all the plots in order to better represent the spatial variability.

temperature (T_{MRT}), and the universal thermal climate index (UTCI) (Lindberg et al., 2008; Lindberg and Grimmond, 2011). T_{MRT} is the equivalent temperature due to exposure to absorbed shortwave and longwave radiation from all directions in a standing position. SOLWEIG was forced using near-surface ERA-5 data. Building, vegetation heights, and digital terrain model were again derived from 3DEP LiDAR point cloud data. Both SUEWS and SOLWEIG were run using the urban multi-scale environment predictor (UMEP) (Lindberg et al., 2018) plug-in with QGIS.

3.4. Social vulnerability index (SoVI)

SoVI employs principal component analysis (PCA) to extract important information from socio-demographic factors from the most recent five-year complete US census data (2015-2020). In this study, we mapped SoVI for each census tract in Austin. The socio-demographic variables used in the PCA analysis are presented in section S2 of the supplementary material. If census data was not available at the tract level, data for the census block group was used. All data used for PCA analysis and calculated SoVI were normalized between 0 and 1 using the maxmin normalization method. Correlation tests were performed before PCA analysis to reduce the data volume, as some socio-demographic factors were autocorrelated in Austin. It should be noted, however, that assumptions about such correlations in other cities may not be valid. By calculating SoVI based solely on socio-demographic data from Austin, we can directly compare SoVI values across different neighborhoods. The map of SoVI in Fig. 4, shows high vulnerability in the eastern part of the city where historically, industries and low-income groups have been located.

4. Results and discussions

The heat hazard analysis presented here encompasses both historical and present-day scenarios. Heat vulnerability estimates, however, are only done for the current conditions, as the estimated SoVI is based on census data from 2015 to 2020.

4.1. Historical heat characterization

In Fig. 5, we analyzed the correlation between MODIS LST and impervious fraction (λ_i) for the years 2004, 2008, 2013, and 2019 as NLCD λ_i was available at a spatial resolution of 30 m for these years. Due to a discrepancy between MODIS LST grid cells and λ_i, we aggregated λ_i within the MODIS grid cell for analysis. The positive correlation between LST and λ_i is a result of urban surface energy balance, reduced sky-view factor for walls and streets, shading, and evaporative cooling due to vegetation. The insets in Fig. 5 depict the data only for summers. The coefficient of determination (r^2) varies over the years, as LST also depends on annual synoptic scale features such as droughts and seasonal changes in the thermal characteristics of rural areas. Here, rural area is classified based on the value of λ_i. The results show that neighborhoods with high λ_i are warmer, but the LST for neighborhoods with smaller λ_i is not necessarily cooler; instead, it depends on interannual variability. For example, during the El Nino years (2004 and 2019) when Austin

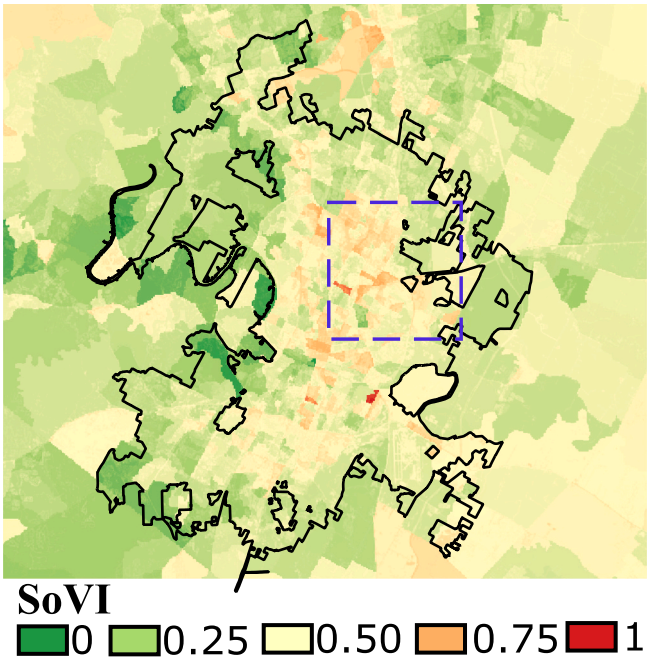

Fig. 4. Social vulnerability index (SoVI) for Austin calculated using US census data from 2015-2020. The box indicates the approximate location of the historically disadvantaged eastern Austin communities.

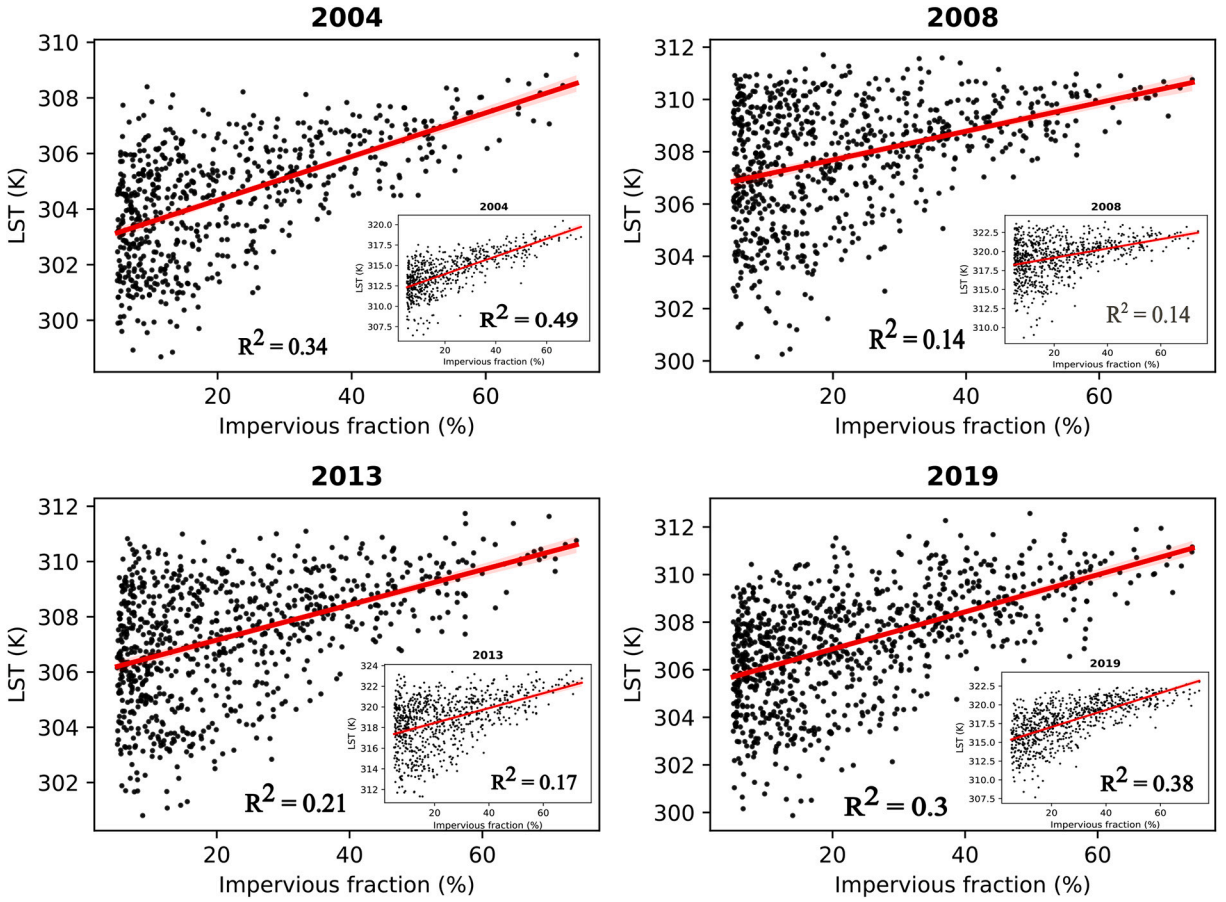

Fig. 5. Scatter plots between impervious fration (λ_i) and MODIS land surface temperature (LST) for the years 2004, 2008, 2013 and 2019. Insets show the data only for summer seasons (June-August).

is wetter than normal with a lower soil moisture deficit, there is a better correlation between λ_i and LST, while during the La-Nina years (2008 and 2013) when it is drier than normal, this correlation is marginally weak, especially during summers. Therefore, we conclude that using surface urban heat island intensity as a proxy for heat hazard can sometimes be misleading, as high urban and rural LSTs during dry conditions may result in a small value of heat island intensity.

Following the approach of Hulley et al. (2019), we produced two additional maps for Austin using MODIS-Aqua LST. The first map shows the average LST on days of heat waves from 2003 to 2020, revealing which areas have historically been subjected to high LST. The second map shows the trend in the number of days in a year with a daily average LST greater than the 95th percentile of climatological value, identifying locations with a rapid increase in LST. We used T2M readings from the Austin Camp Mabry weather station and the excess heat factor (EHF) approach (Nairn and Fawcett, 2014) to detect heatwave episodes to create the first map. Camp

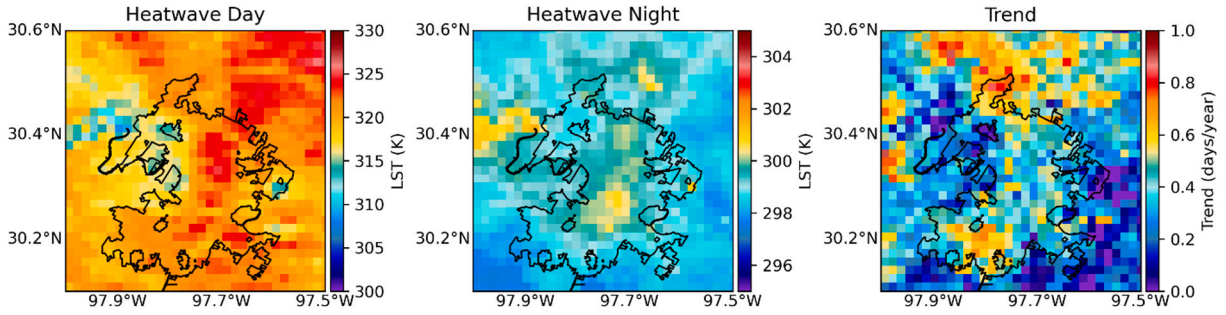

Fig. 6. MODIS-derived mean land surface temperature (LST) during heatwave day and night (left and center). Trend in number of days with LST exceeding the 95th percentile of mean day-time temperature for the period 2003 and 2020 (right). Note the different temperature scales for day- and night-time LST plots; this, was done to highlight the spatial variability.

Mabry is an operational, urban representative station, with $\lambda_i = 0.34$, $\lambda_v = 0.58$ and bare soil $(\lambda_{bc}) = 0.08$ within a 400-m vicinity. The EHF method compares the 3-day averaged daily mean temperature with the 95th percentile of climatological values and also considers the acclimatization factor calculated by comparing the 3-day averaged mean daily temperature with the mean temperature of the past 30 days. We chose heatwave days because they are often associated with anticyclonic and dry weather conditions that bring clear skies and calm conditions, ideal for urban temperature studies. Fig. 6 shows the spatial maps of daytime and nighttime LST during heatwaves along with the spatial trend for increasing hot days in Austin.

Fig. 6 shows that most of the built-up areas of Austin, as shown in the LCZs of Fig. 1, are warmer during the day, while downtown Austin is hotter during the night. This is due to the tall buildings in downtown that reduce the sky-view factor and increased storage and anthropogenic heat flux, leading to reduced cooling efficiency. Additionally, the northeastern part of Austin is hot during the day as this region turns into bare soil under dry conditions. However, most LCZ classifiers mark this area as LCZ_D. Thus, if we use the definition of surface heat island intensity by Bechtel et al. (2019) during dry conditions, we will see that Austin shows a small heat island intensity or may even exhibit an urban cool island effect. This discussion supports the argument of using heat island intensity for heat assessment from Fig. 5 and reinforces the role of rural characteristics.

The trend plot shows that the northern and southern neighborhoods of the city are experiencing the most rapid increase in LST, which is consistent given the city's sprawl in these directions. Fig. 6 also illustrates that Austin's LST is increasing on average.

4.2. Present-day heat characterization

Vehicle traverse data is used to show the T2M anomaly for each LCZ in Fig. 7b. Each LCZ's mean T2M was subtracted from the traverse's overall mean T2M to calculate the anomaly. As can be seen in Fig. 7b, urban areas tend to be warmer than their rural counterparts. Fig. 7a shows that the value of T2M is very stable during the afternoon when heat stress is normally at its peak. This is because the urban and rural areas are warmed almost equally by mid-afternoon. However, the highest anomaly was observed during the morning, likely due to the thermal properties of urban features, reduced sky-view factor, and anthropogenic heat flux. Overall, the LCZ approach provides a useful framework for analyzing microclimates within urban areas (Ching et al., 2018; Stewart and Oke, 2012).

Fig. 7 also shows that it is possible to get the wrong conclusions when relying on temperature anomalies or canopy urban heat island intensity (CUHII) for heat vulnerability assessments. The intensity of CUHII decreases significantly towards the afternoon, suggesting that the UHI effect is lessened at this time. Conversely, the CUHII is highest during the early morning. If one were to rely solely on CUHII as an indicator for heat vulnerability, one would mistakenly conclude that early morning is when mitigation efforts are necessary. However, during mornings, the temperature is approximately 297 K (23.85 °C), which is considered comfortable, and therefore does not necessarily require mitigation. On the other hand, in the afternoon, when the CUHII is at its minimum, the temperatures rise to around 309 K (35.85 °C), indicating the need for heat mitigation measures.

4.3. Heat vulnerability index (HVI)

A preliminary analysis of HVI was done using normalized ECOSTRESS LST as a hazard as it offers large geographical coverage. HVI was calculated as

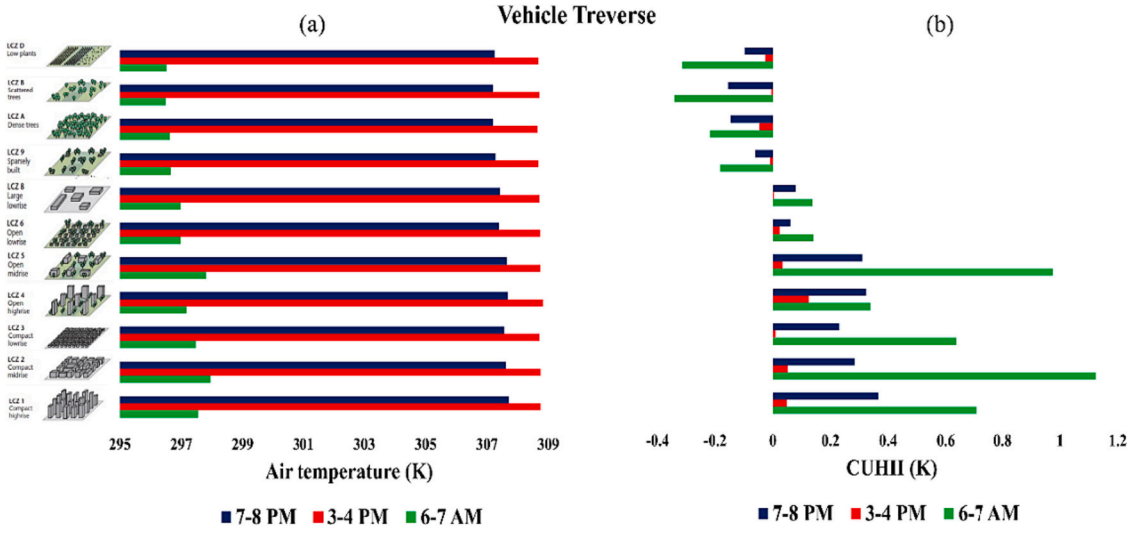

Fig. 7. (a) 2-meter air temperature (T2M) and (b) temperature anomalies (or canopy urban heat island intensity- CUHII) for different local climate zones (LCZs) in Austin. Figure style adopted from (Stewart and Oke, 2012).

$$\mathrm{HVI} = \mathrm{LST_N(heat\ \ hazard)} \times \mathrm{SoVI} \quad (1)$$

We computed the ECOSTRESS HVI for four summertime daytime scenarios separated by around six hours to find neighborhoods that are typically at risk all day long. Fig. 8 shows the results for the 95th percentile of HVI, highlighting the vulnerable neighborhoods. For further analysis, we considered one neighborhood (Rundberg) that is highlighted using a circle in Fig. 8. It should be noted that although certain areas of downtown Austin experience high LST, they do not appear in Fig. 8 due to their lower SoVI owed to higher adaptive capacity. Additionally, another location with a lower SoVI was identified in West Austin. The three neighborhoods (Rundberg, downtown and West Austin) discussed are marked in Fig. 1a, and later sections provide a more detailed analysis of these areas using a model.

4.3.1. *Comparison of HVI calculated using LST and T2M*

The LST recorded by space-borne sensors may not be representative of the temperatures experienced by humans. Therefore, to assess heat vulnerability, it is necessary to use T2M. As many previous studies in the literature have used LST to quantify heat vulnerability, for instance, Hulley et al. (2019), it is crucial to compare the HVIs calculated using ECOSTRESS LST and mobile traverse T2M to understand the spatial patterns and magnitudes of HVI calculated using the two hazards. Fig. 9 presents this comparison.

To make a meaningful comparison between the ECOSTRESS LST data recorded in different years during the summer season and the vehicle traverse T2M in the morning and evening of 7th August 2020, we normalized the data before calculating HVI. Although the afternoon data is presented in Fig. 9 for illustrative purposes, it cannot be compared directly to T2M because of the time difference. During the morning period, the magnitude of HVI calculated using T2M is higher than that based on LST. This is because the roofs are cooler in the morning, but T2M inside the urban canyon is warmer due to longwave emissions from the walls. However, during the

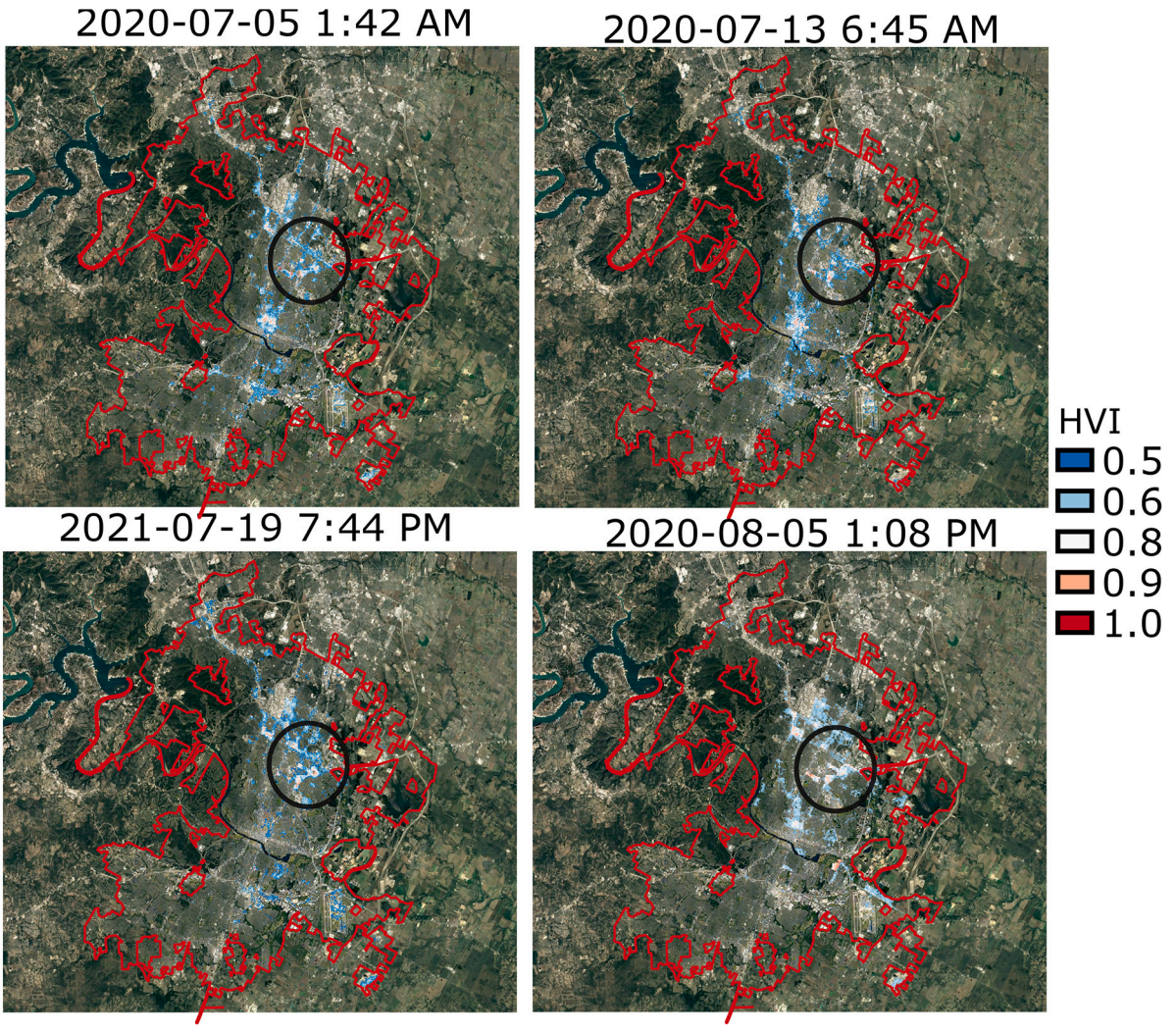

Fig. 8. 95th percentile of heat vulnerability index (HVI) calculated using normalized ECOSTRESS land surface temperature (LST). The black circle shows the Rundberg neighborhood in northeast Austin that has high social vulnerablity.

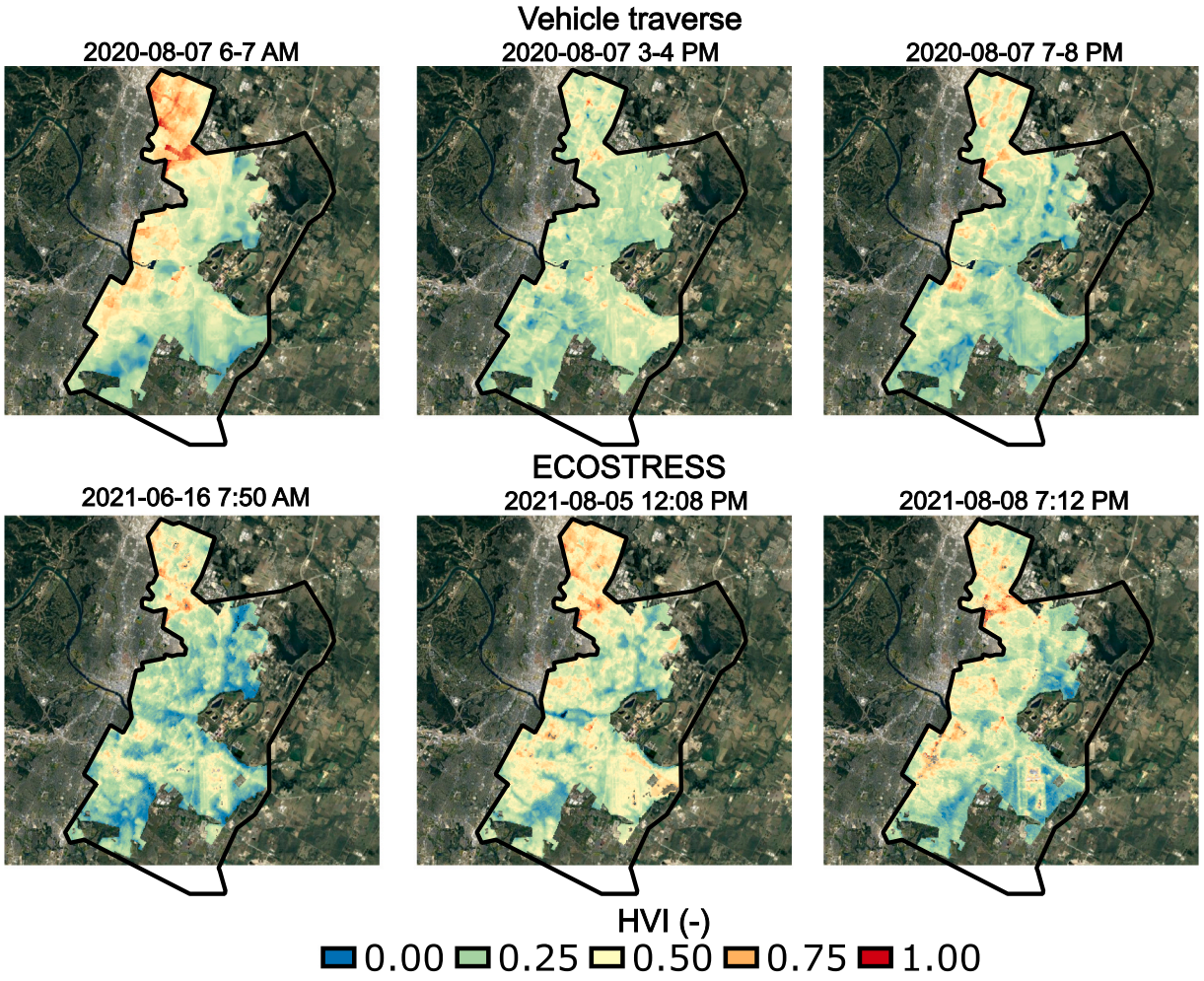

Fig. 9. Comparison of heat vulnerablity index (HVI) calculated using vehicle traverse 2-meter air temperature (top row) and ECOSTRESS land surface temperature (bottom row) as heat hazards.

other two times of the day, the LST-based HVI is overestimated in many neighborhoods, as the value of LST is typically higher than T2M (Christen et al., 2012; Voogt and Oke, 2003).

4.4. The daytime human heat health index (H3I)

It is evident from Fig. 9 that HVI can only be utilized to compare vulnerability between different neighborhoods at a given time and does not provide information on the actual vulnerability. For example, the value of vehicle traverse-based HVI is high in the morning at Rundberg, but by examining the value of T2M (Figure 7), we find that the heat stress is minimal. Therefore, to comprehend urban heat vulnerability, the diurnal profile of National Weather Service heat index (HI) (in °F) that uses both temperature and RH must be considered. We introduce a new definition of heat hazard as follows:

$$\mathrm{H} = \sum_{\mathrm{i}} \{max((\mathrm{HI_i} - 101), 0)\} \tag{2}$$

The proposed definition of heat hazard is 'H', where 'i' is the hour of the day, and the value 101 °F is based on the National Weather Service threshold of 'dangerous heat'. H considers the cumulative hours when the heat index exceeds the dangerous heat limit, allowing for a direct comparison of absolute daytime heat hazard between different neighborhoods. In addition, the definition of HVI was modified to account for H, resulting in the definition of the daytime human heat health index (H3I).

$$\mathrm{H3I} = \mathrm{H} \times \mathrm{SoVI} \tag{3}$$

The weather observations required to calculate H3I for different LCZs were not available in Austin. Therefore, we relied on SUEWS simulations.

4.5. SUEWS simulations

The SUEWS domain was set up at three locations, as marked in Fig. 1a, with a 1-h time step for the entire year 2020. As noted in study by Best and Grimmond (2013), soil moisture initialization affects temperature outcomes. Thus, we ran the model for the first 8 months of the year 2020 as a spin-up phase. Our goal in using the SUEWS was to disentangle the separate impacts of HI and SoVI on H3I. For this, first we simulated T2M and relative humidity at Austin Camp Mabry weather station neighborhood for validation of the SUEWS model. T2M simulation results showed good overall agreement when compared with measurements (Fig. S3 in supplementary material). The Google Earth imagery of the modeled neighborhoods is presented in Fig. 10, along with the SUEWS-simulated hourly averaged surface energy balance components in the inertial sublayer for July 1 to August 31, 2020 (dry period) and heat index for a hot day, August 12, 2020. The modeled anthropogenic heat flux was highest in downtown, attributed to its higher population density and traffic. Note that we used the same cut-off values of temperatures for heating and cooling to calculate anthropogenic heat in SUEWS as in, Tang et al. (2021). This introduces some uncertainty, but the impact is expected to be small.The modeled latent heat flux was small due to a significant dry surface conditions. There was intermittent precipitation during the afternoons in Austin, leading to the mean diurnal profile of latent heat flux skewed towards the evening period. Note that the sensible heat flux is always positive in downtown. This can be attributed to the presence of mechanically driven turbulence and large storage and anthropogenic heat fluxes during the night. The heat index was greater than the National Weather Service-designated 'dangerous' heat limit line for approximately 5–6 h in the three modeled neighborhoods.

The values for H, SoVI, and H3I for the three areas are shown in Table 1. Due to possible model and/or boundary forcing uncertainties, simulated T2M results did not capture the nocturnal UHI effect in the downtown area when compared with lower built-up types with more vegetation fraction (as shown in Fig. 7). Our focus here, however, is to demonstrate how H3I accounts for the duration and severity of heat-vulnerable periods. In this scenario, a comparison of H values across different areas reveals that downtown is subject to the least amount of heat. When the heat vulnerability of these three areas is compared using the H3I, we find that Rundberg area is the most at heat risk. By examining T2M and SoVI individually, we find that SoVI has a large influence on H3I. For instance, a neighborhood with high hazard and low SoVI may not be categorized as vulnerable, while a neighborhood with moderate heat hazard and high SoVI may be classified as highly vulnerable. Another limitation of using the local-scale H3I calculated using heat index is that it does not resolve heat vulnerability within the neighborhood, which is sometimes needed for planning intervention strategies.

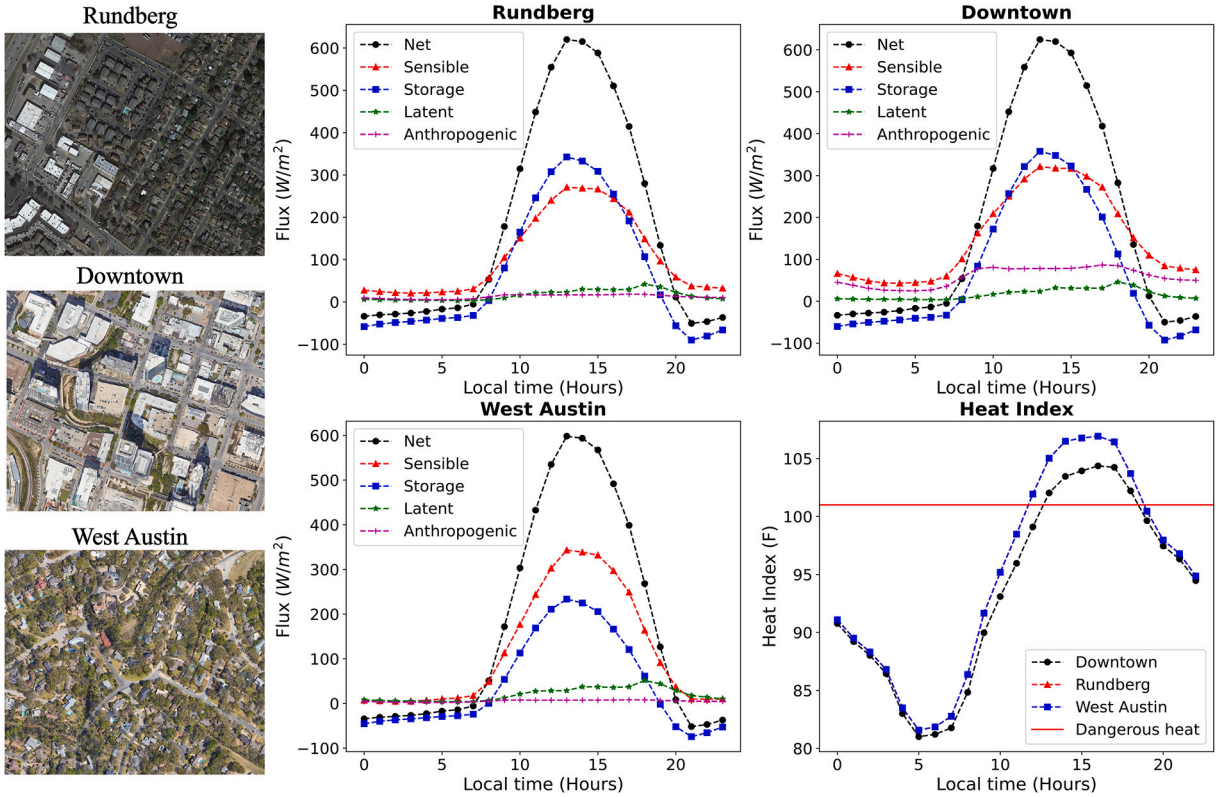

Fig. 10. Surface energy balance (SEB) at Rundberg (λ_v=0.2, λ_b=0.23, λ_{pa} = 0.51), downtown (λ_v=0.08, λ_b=0.4, λ_{pa} = 0.44) and west Austin (λ_v=0.58, λ_b=0.17, λ_{pa} = 0.2) in 400-meter vicinity. λ_{pa} is the paved fraction. Modeled heat index (HI) and NWS 'dangerous heat' limit is also shown.

Table 1
Calculated heat hazard (H) and human heat health index (H3I) along with social vulnerability index for the three simulated neighborhoods.

	H	SoVI	H3I
Rundberg	30.3	0.61	18.5
Downtown	14.25	0.29	4.1
West Austin	31.3	0.44	13.8

5. H3I for human heat health assessment and planning of heat mitigation strategies

The H3I calculated using heat index (as a heat hazard) provides a means of quantifying and comparing absolute heat vulnerability across different neighborhoods. However, it is not directly applicable for planning heat mitigation strategies because it does not provide insights into locating interventions (e.g., trees or bus shelters) for heat mitigation or for assessing to what extent the mitigation strategy has been successful in reducing heat stress. Such data can be obtained by street-scale modeling, and is discussed ahead. We suggest utilizing universal thermal climate index (UTCI) to evaluate heat hazard when developing heat mitigation strategies. UTCI is a function of mean radiant temperature (T_{MRT}), T2M, wind speed, and humidity. Street vegetation and buildings are strongly linked to T_{MRT} and UTCI due to the shading effect.

For street scale analysis, we employed SOLWEIG to model T_{MRT} and UTCI at two neighborhoods with different SoVI for a clear-sky summer day (August 12, 2020). The building raster was simplified to level of detail-1 for modeling simplicity and wind speed was taken as 2 m/s while temperature and relative humidity was taken from the meteorological forcing data. Fig. 11 displays a Google Earth image and modeled T_{MRT} at three different times of day to emphasize the importance of incorporating 3-D urban data in street-level heat hazard modeling.

For the analysis of T_{MRT} and UTCI, we selected six points (P1-P6) at location-1 and four points (P1-P4) at location-2, as indicated in Fig. 11. These points were chosen based on the different sky view factors. Fig. 12 shows the diurnal patterns of T_{MRT} and UTCI at these points. Depending on the points' relative location to the tree canopy or buildings, shading occurs at different times of the day. For example, point P5 at location-1 experiences lower T_{MRT} before the sub-solar point due to the shading provided by the nearby tree compared to point P3, where SVF = ~1.

We calculated the hazard using UTCI at all points in both locations. A value of UTCI $\geq$32 °C was chosen as a cut-off for heat hazard calculation in eq. 2 as it indicates strong heat stress (Bröde et al., 2012). The results of our calculations for heat hazard and H3I are presented in Table 2. The table shows that the surrounding infrastructure can reduce heat hazard by approximately 27% for point P4 at location 1 and 25% for point P3 at location 2 compared to the points with open-sky. The corresponding reductions in H3I were 26.3% and 25.1%, respectively. In the present case, the values of heat hazard and H3I reduction are mostly similar as the comparison is for the neighborhoods with same SoVI. However, when comparing neighborhoods with different SoVI, this difference can be large. Such

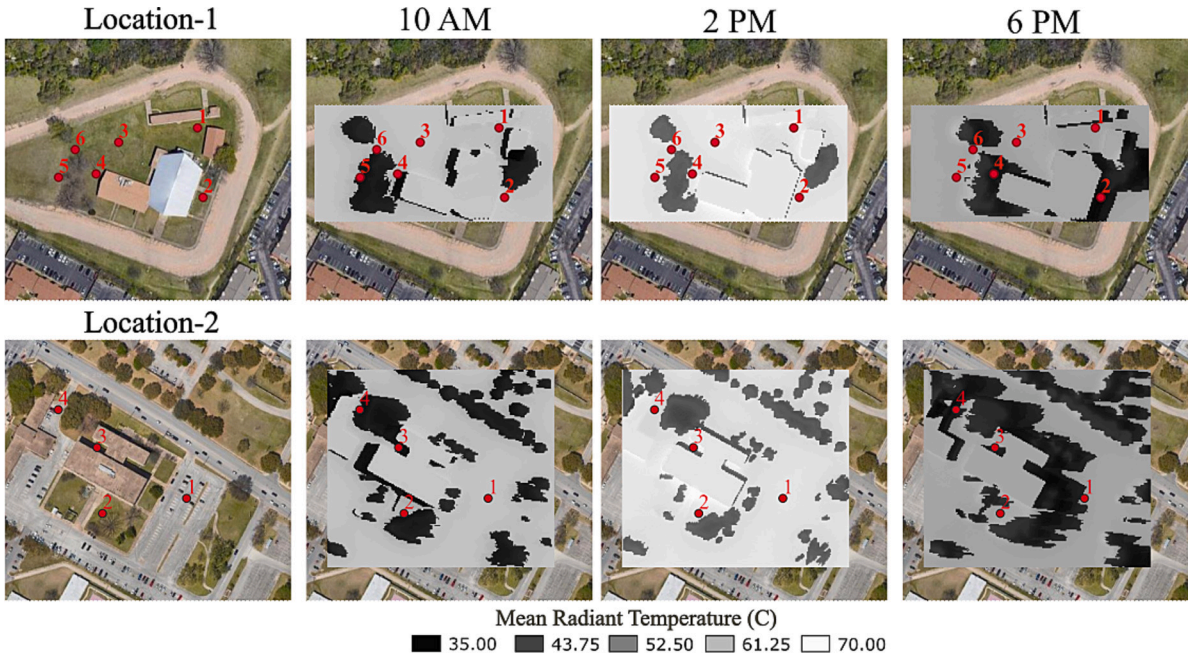

Fig. 11. Modeled mean radiant temperature (T_{MRT}) at two neighborhoods in Austin. Different points (P1-P6 at location 1 and P1-P4 at location 2) were chosen for analysis based on the sky view factors and are also shown.

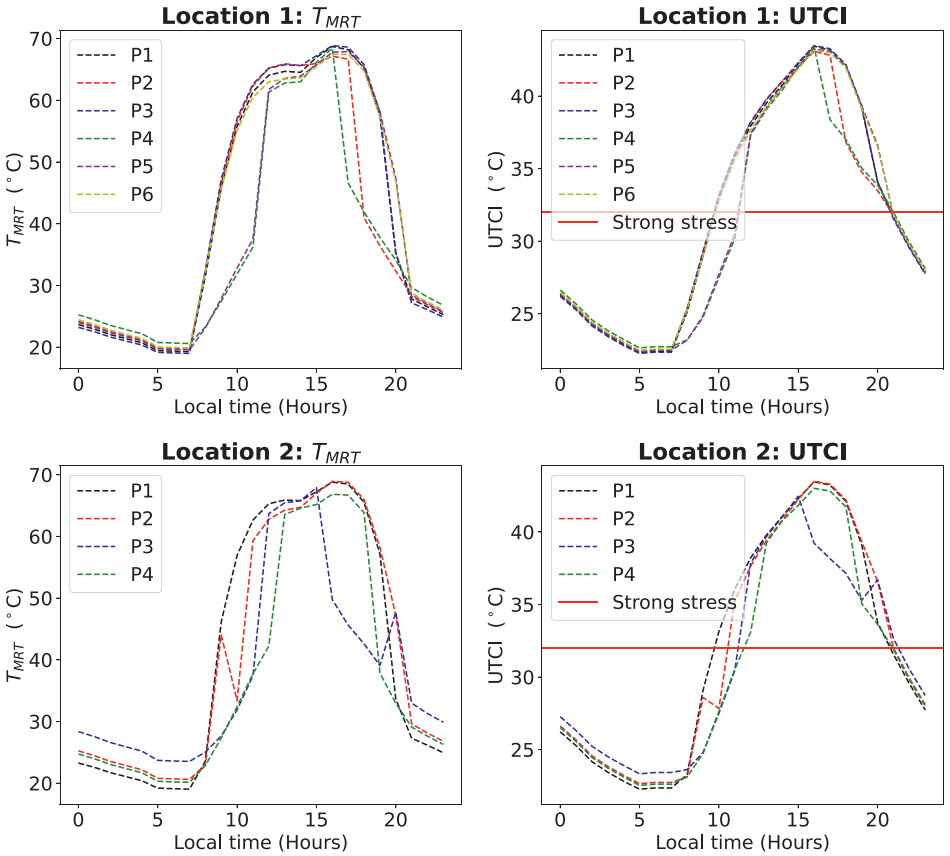

Fig. 12. T_{MRT} and universal thermal climate index (UTCI) at the selected points at the two locations. Strong heat stress limit (UTCI≥32 °C) is also shown. The points P1-P6 at location 1 and points P1-P4 at location 2 are shown in Fig. 11.

Table 2
Calculated heat hazard (H) and human heat health index (H3I) for different sky view factors at location 1 (points P1-P6) and location 2 (points P1-P4) as shown in Fig. 11. Social vulnerability index (SoVI) for the two locations is also shown. Heat hazard reduction was calculated using P3 at location 1 and P2 at location 2 as reference. These points represent a sky view factors of ~1.

Location 1						Location 2					
Point	H	SoVI	Hazard reduced	H3I	H3I reduced	Point	H	SoVI	Hazard reduced	H3I	H3I reduced
P1	79	0.53	1.3%	41.9	0.5%	P1	80.2	0.32	0.2%	28.1	0.2%
P2	69		13.8%	36.6	13.1%	P2	80.4		–	28.1	–
P3	80		–	42.4	−0.8%	P3	60.2		25.0%	21.1	25.1%
P4	58.5		26.9%	31.0	26.3%	P4	63.2		21.3%	22.1	21.4%
P5	75.6		5.5%	40.1	4.7%						
P6	79.37		0.8%	42.1	–						

information is expected help the planning of heat mitigation strategies. Additionally, H3I allows us to perform if-then analyses to evaluate the efficacy of implemented intervention strategies. In other words, planners can use H3I to evaluate how effective different strategies can be in reducing heat stress for specific locations.

5.1. *Alternate definitions of H3I*

Another measure of human thermal comfort that considers 3-D urban geometry is the physiological equivalent temperature (PET) (Höppe, 1999). PET takes into account factors such as T2M, relative humidity, wind speed, as well as human characteristics including height, weight, gender, clothing, and energy expenditure during activity. H3I can also be defined based on PET for assessing thermal comfort and planning heat mitigation strategies. This can be achieved by modifying the hazard calculation using a PET cutoff of 35 °C, which indicates strong heat stress. Alternatively, the hazard can be determined based on the fraction of the day when UTCI or PET exceeds 32 °C or 35 °C, respectively. To illustrate the hazard defined using the time fraction, spatial maps of UTCI and PET were

calculated for August 12, 2020, at location 2 shown in Fig. 11. These maps are shown in Fig. 13. It is important to account for wind speed when calculating UTCI and PET spatially, as buildings and trees can act as obstacles and change wind speeds in their vicinity. In this study, the urban wind field processor (Bernard et al., 2023) in UMEP was utilized to calculate the wind field, assuming unobstructed winds at a height of 10 m flowing at 2 m/s from the northeast direction. PET was computed for a 35-year-old male weighing 75 kg, engaged in an activity spending 80 W.

Fig. 13 additionally presents the average daytime UTCI and PET. As the simulated wind flow is considered to be from the northeast, the wind speed in the southwest region of the building (highlighted as a black box in Fig. 13) is nearly zero. This low wind speed has a greater impact on PET compared to UTCI, showing higher sensitivity. Observing the results, it is evident that the daily mean PET reaches its peak in areas with open sky and negligible wind speed, whereas UTCI closely aligns with the shading effect due to buildings and trees.

5.2. The community factor in H3I

The urban heat mitigation process is an iterative approach that requires validation and correction of modeled vulnerable areas based on community feedback (Bixler et al., 2022). To gather this feedback, residents of the Rundberg neighborhood (as shown in Figure 8) were asked about their heat experiences in the surrounding area. The interpolated vehicle traversed T2M for the afternoon period (3–4 PM) was used to investigate the spatial correlation between air temperature and community perception of heat. While individuals may have different tolerance levels for heat, the objective was to identify any heat hotspots based on community experiences. The residents were also asked about their preferred heat mitigation strategies and where they would like to see them implemented. Fig. 14 shows the results for both community perception of heat and potential locations for heat mitigation strategy implementation.

The findings in Fig. 14 demonstrate that higher T2M does not necessarily indicate higher heat hazard according to community perception. Rather, hazard and heat mitigation strategies appear to be focused on areas that people visit frequently. This underscores the significance of community engagement in heat mitigation planning (Lanza et al., 2023). To accommodate resident mobility, it may be necessary to adjust the definition of H3I.

$$\mathrm{H3I} = \mathrm{SoVI} \times \sum_{i} \{max(\mathrm{UTCI_i} - 32), 0\} \times \mathrm{E_i} \tag{4}$$

This modified definition of H3I accounts for resident mobility and enables the prioritization of heat mitigation strategies based on the probability of resident visits to a neighborhood at a given time (E_i). E_i can therefore be considered as exposure.

5.3. Final remarks on H3I

It is important to consider community input and the suitability of the chosen heat mitigation strategy for the neighborhood. For example, implementing green infrastructure in water-stressed areas may not be feasible, and alternative strategies such as bus shelters or cool pavements and roofs may be necessary. In brief, to effectively address daytime urban heat vulnerability, it is important to account for the urban 3-D features, social vulnerability, and community feedback in a comprehensive modeling framework. This approach will allow for the identification and implementation of appropriate heat mitigation strategies that are tailored to the specific needs and characteristics of the community.

6. Conclusions

Recent space-borne sensors, such as ECOSTRESS, allow for high spatio-temporal analysis of LST. They are useful for conducting a preliminary assessment of heat vulnerability as they provide large geographical coverage. Calculation of UHI intensity using LST is generally errorneous and misleading (Mills et al., 2022) and estimation of UHI from T2M is necessarily dependent on rural characteristics. Therefore, using UHI intensity to plan heat mitigation strategies at times can be misleading as it only highlights whether the urban surface is relatively warmer or cooler than the corresponding rural area. In this paper, we highlight that heat hazard must consider 3-D urban features, aided by social vulnerability and community feedback, within a modeling framework to co-produce and implement appropriate heat mitigation strategies.

When using remotely sensed LST as a hazard to calculate HVI, caution must be exercised as the satellite sensor does not capture the complete urban surface. As a result, when compared to HVI calculated using T2M, the HVI derived from LST can be overestimated during mid-day times. Furthermore, spatial maps of HVI provide relative vulnerability information that is valid for that time and for a neighborhood relative to others. Therefore, to determine the absolute vulnerability of a neighborhood, we need the diurnal profile of heat hazard. Accordingly, we defined a new heat hazard metric that considers the magnitude of heat index and the cumulative hours of the day when heat index exceeds a prescribed threshold. Combining this hazard metric with social vulnerability yielded a new index, human heat health index (H3I), which was found to be a more robust method for understanding neighborhood-scale absolute vulnerability.

To plan and evaluate the effectiveness of heat mitigation strategies, street-level modeling is effective as it considers the shading effect of buildings and trees. Using modeled universal thermal climate index at the street-level as a heat hazard, we calculated H3I at different points for varying sky view factors to investigate how built and green infrastructure affect H3I. Our findings indicated that locations adjacent to trees have a varying impact on cooling, and a reduction of approximately 25% in heat hazard compared to a

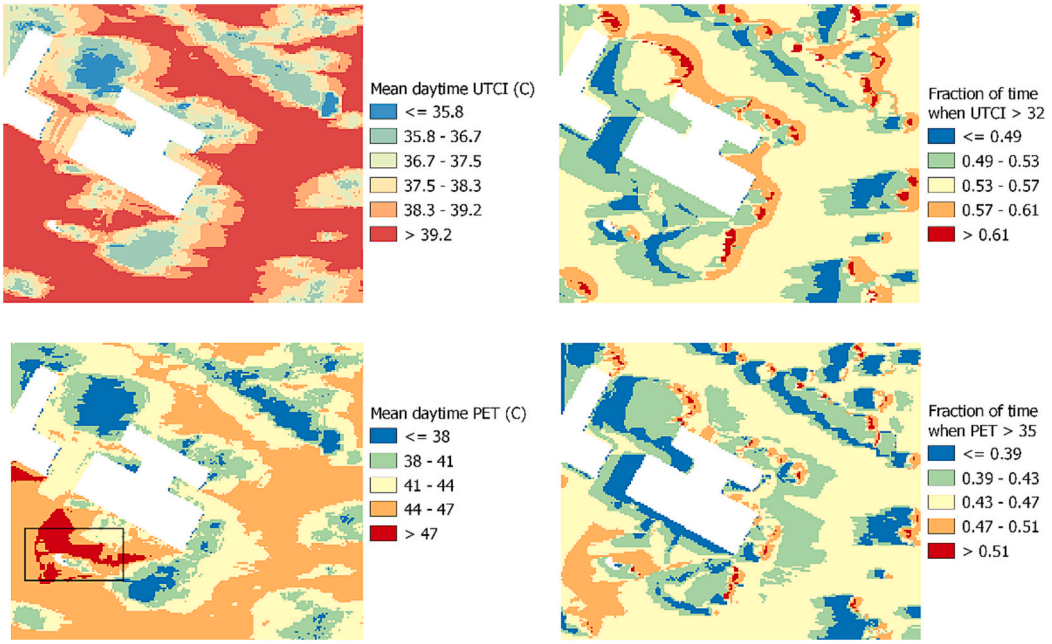

Fig. 13. Mean daytime universal thermal climate index (UTCI) and physiological equivalent temperature (PET) in °C and the fraction of time during the entire day (24-h) when UTCI >32 °C and PET >35 °C at location 2 as shown in Fig. 11.

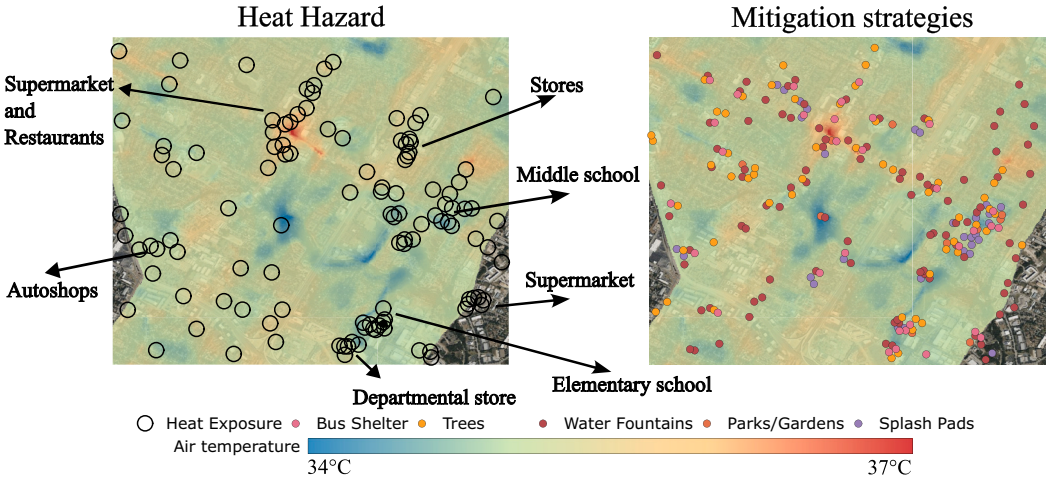

Fig. 14. Community perception of heat hazard and suggested mitigation strategies near the Rundberg neighborhood. Basemap shows vehicle traverse 2-meter temperature during the afternoon (3-4 PM).

location with an open sky. Furthermore, our study emphasized the importance of involving the community in decision-making for heat mitigation, as the modeled heat hazard may not always align with the public perception of heat. We introduced a time-varying exposure, E_i, in heat mitigation studies using a simple community heat hazard dataset that was obtained from a survey. However, currently we do not have estimates of E_i for different cities, and will be a subject of future research. One possible approach we are exploring to generate a temporally varying E_i is by generating a synthetic population data (Macal et al., 2018).

Funding

National Oceanic and Atmospheric Administration (NOAA) National Integrated Heat Health Information System (NIHHIS) [NA21OAR4310146, NOAA/CPO #100007298], National Aeronautics and Space Administration (NASA) Interdisciplinary Research in Earth Science (IDS) [80NSSC20K1262 and 80NSSC20K1268], U. S. National Science Foundation (NSF) [OAC-1835739], National Institute of Environmental Health Sciences (NIEHS) [K01ES034382], NASA's Earth Science Division Equity and Environmental Justice

(EEJ) program [80NSSC22K1675], University of Texas at Austin (UT) Jackson School of Geosciences: Farish Chair to DN and Presidential Endowed Fellowship to HK, and Oden Institute of Computational Engineering and Sciences, and UT's JT Oden Faculty Fellowship Research Program to AM.

Declaration of generative AI and AI-assisted technologies in the writing process

During the preparation of this work the author(s) used chatGPT in order to check grammar and paraphrasing. After using this tool/service, the author(s) reviewed and edited the content as needed and take(s) full responsibility for the content of the publication.

CRediT authorship contribution statement

Harsh G. Kamath: Conceptualization, Methodology, Software, Formal analysis, Data curation, Writing – original draft. **Alberto Martilli:** Methodology, Formal analysis, Investigation, Writing – review & editing. **Manmeet Singh:** Formal analysis, Writing – review & editing. **Trevor Brooks:** Formal analysis, Writing – review & editing. **Kevin Lanza:** Data curation, Writing – review & editing. **R. Patrick Bixler:** Investigation, Resources, Writing – review & editing. **Marc Coudert:** Data curation, Supervision, Investigation, Project administration. **Zong-Liang Yang:** Supervision, Writing – review & editing. **Dev Niyogi:** Conceptualization, Methodology, Supervision, Writing – review & editing, Funding acquisition.

Declaration of Competing Interest

The authors declare that there is no competing interest in any form.

Data availability

Data will be made available on request.

Appendix A. Supplementary data

Supplementary data to this article can be found online at https://doi.org/10.1016/j.uclim.2023.101675.

References

Bechtel, B., Demuzere, M., Mills, G., Zhan, W., Sismanidis, P., Small, C., Voogt, J., 2019. SUHI analysis using local climate zones—a comparison of 50 cities. Urban Clim. 28, 100451 https://doi.org/10.1016/j.uclim.2019.01.005.

Beck, H.E., Zimmermann, N.E., McVicar, T.R., Vergopolan, N., Berg, A., Wood, E.F., 2018. Present and future köppen-Geiger climate classification maps at 1-km resolution. Sci. Data 5. https://doi.org/10.1038/sdata.2018.214.

Bernard, J., Lindberg, F., Oswald, S., 2023. URock 2023a: An Open Source GIS-Based Wind Model for Complex Urban Settings. https://doi.org/10.5194/egusphere-2023-354.

Best, M.J., Grimmond, C.S.B., 2013. Analysis of the seasonal cycle within the first international urban land-surface model comparison. Bound.-Layer Meteorol. 146, 421–446. https://doi.org/10.1007/s10546-012-9769-7.

Bixler, R.P., Coudert, M., Richter, S.M., Jones, J.M., Llanes Pulido, C., Akhavan, N., Bartos, M., Passalacqua, P., Niyogi, D., 2022. Reflexive co-production for urban resilience: Guiding framework and experiences from Austin, Texas. Frontiers in Sustainable Cities 4. https://doi.org/10.3389/frsc.2022.1015630.

Bröde, P., Fiala, D., Błażejczyk, K., Holmér, I., Jendritzky, G., Kampmann, B., Tinz, B., Havenith, G., 2012. Deriving the operational procedure for the universal thermal climate index (UTCI). Int. J. Biometeorol. 56, 481–494. https://doi.org/10.1007/s00484-011-0454-1.

Ching, J., Mills, G., Bechtel, B., See, L., Feddema, J., Wang, X., Ren, C., Brorousse, O., Martilli, A., Neophytou, M., Mouzourides, P., Stewart, I., Hanna, A., Ng, E., Foley, M., Alexander, P., Aliaga, D., Niyogi, D., Shreevastava, A., Bhalachandran, P., Masson, V., Hidalgo, J., Fung, J., Andrade, M., Baklanov, A., Dai, W., Milcinski, G., Demuzere, M., Brunsell, N., Pesaresi, M., Miao, S., Mu, Q., Chen, F., Theeuwesits, N., 2018. WUDAPT: an urban weather, climate, and environmental modeling infrastructure for the anthropocene. Bull. Am. Meteorol. Soc. 99, 1907–1924. https://doi.org/10.1175/BAMS-D-16-0236.1.

Chow, W.T.L., Roth, M., 2006. Temporal dynamics of the urban heat island of Singapore. Int. J. Climatol. 26, 2243–2260. https://doi.org/10.1002/joc.1364.

Christen, A., Meier, F., Scherer, D., 2012. High-frequency fluctuations of surface temperatures in an urban environment. Theor. Appl. Climatol. 108, 301–324. https://doi.org/10.1007/s00704-011-0521-x.

Cutter, S.L., Boruff, B.J., Shirley, W.L., 2003. Social vulnerability to environmental hazards. Soc. Sci. Q. 84, 242–261. https://doi.org/10.1111/1540-6237.8402002.

Fung, K.Y., Yang, Z.-L., Niyogi, D., 2022. Improving the local climate zone classification with building height, imperviousness, and machine learning for urban models. Comput. Urban Sci. 2 https://doi.org/10.1007/s43762-022-00046-x.

Höppe, P., 1999. The physiological equivalent temperature - a universal index for the biometeorological assessment of the thermal environment. Int. J. Biometeorol. 43, 71–75. https://doi.org/10.1007/s004840050118.

Hulley, G., Shivers, S., Wetherley, E., Cudd, R., 2019. New ECOSTRESS and MODIS land surface temperature data reveal fine-scale heat vulnerability in cities: a case study for Los Angeles County, California. Remote Sens. 11, 6–8. https://doi.org/10.3390/rs11182136.

Järvi, L., Grimmond, C.S.B., Christen, A., 2011. The surface urban energy and water balance scheme (SUEWS): evaluation in Los Angeles and Vancouver. J. Hydrol. (Amst.) 411, 219–237. https://doi.org/10.1016/j.jhydrol.2011.10.001.

Jendritzky, G., de Dear, R., Havenith, G., 2012. UTCI-why another thermal index? Int. J. Biometeorol. 56, 421–428. https://doi.org/10.1007/s00484-011-0513-7.

Krayenhoff, E.S., Voogt, J.A., 2010. Impacts of urban albedo increase on local air temperature at daily-annual time scales: model results and synthesis of previous work. J. Appl. Meteorol. Climatol. 49, 1634–1648. https://doi.org/10.1175/2010JAMC2356.1.

Laaidi, K., Zeghnoun, A., Dousset, B., Bretin, P., Vandentorren, S., Giraudet, E., Beaudeau, P., 2012. The impact of heat islands on mortality in Paris during the august 2003 heat wave. Environ. Health Perspect. 120, 254–259. https://doi.org/10.1289/ehp.1103532.

Lanza, K., Jones, J., Acuña, F., Coudert, M., Bixler, R.P., Kamath, H., Niyogi, D., 2023. Heat vulnerability of Latino and Black residents in a low-income community and their recommended adaptation strategies: A qualitative study. Urban Clim. 51. https://doi.org/10.1016/j.uclim.2023.101656.

Lindberg, F., Grimmond, C.S.B., 2011. The influence of vegetation and building morphology on shadow patterns and mean radiant temperatures in urban areas: model development and evaluation. Theor. Appl. Climatol. 105, 311–323. https://doi.org/10.1007/s00704-010-0382-8.
Lindberg, F., Holmer, B., Thorsson, S., 2008. SOLWEIG 1.0 - modelling spatial variations of 3D radiant fluxes and mean radiant temperature in complex urban settings. Int. J. Biometeorol. 52, 697–713. https://doi.org/10.1007/s00484-008-0162-7.
Lindberg, F., Grimmond, C.S.B., Gabey, A., Huang, B., Kent, C.W., Sun, T., Theeuwes, N.E., Järvi, L., Ward, H.C., Capel-Timms, I., Chang, Y., Jonsson, P., Krave, N., Liu, D., Meyer, D., Olofson, K.F.G., Tan, J., Wästberg, D., Xue, L., Zhang, Z., 2018. Urban multi-scale environmental predictor (UMEP): an integrated tool for city-based climate services. Environ. Model. Softw. 99, 70–87. https://doi.org/10.1016/j.envsoft.2017.09.020.
Macal, C.M., Collier, N.T., Ozik, J., Tatara, E.R., Murphy, J.T., 2018. CHISIM: an agent-based simulation model of social interactions in a large urban area. In: 2018 Winter Simulation Conference (WSC). IEEE, pp. 810–820. https://doi.org/10.1109/WSC.2018.8632409.
Martilli, A., Krayenhoff, E.S., Nazarian, N., 2020. Is the urban Heat Island intensity relevant for heat mitigation studies? Urban Clim. 31 https://doi.org/10.1016/j.uclim.2019.100541.
Mills, G., Stewart, I.D., Niyogi, D., 2022. The origins of modern urban climate science: reflections on 'A numerical model of the urban heat island. Progress in Physical Geography: Earth and Environment 46 (4), 649–656.
Nairn, J.R., Fawcett, R.J.B., 2014. The excess heat factor: a metric for heatwave intensity and its use in classifying heatwave severity. Int. J. Environ. Res. Public Health 12, 227–253. https://doi.org/10.3390/ijerph120100227.
NASA SEDAC, 2018. Gridded Population of the World, Version 4 (GPWv4) [WWW Document]. Center for International Earth Science Information Network - CIESIN - Columbia University.
Niyogi, D., Holt, T., Zhong, S., Pyle, P.C., Basara, J., 2006. Urban and land surface effects on the 30 July 2003 mesoscale convective system event observed in the southern Great Plains. J. Geophys. Res. Atmos. 111 (D19).
NOAA, 2021. Weather Related Fatality and Injury Statistics [WWW Document]. URL. https://www.weather.gov/hazstat/ (accessed 4.21.23).
Oke, T.R., 1982. The energetic basis of the urban heat island. Q. J. R. Meteorol. Soc. 108, 1–24. https://doi.org/10.1002/qj.49710845502.
Oke, T.R., Mills, G., Christen, A., Voogt, J.A., 2017. Urban Climates. Cambridge University Press. https://doi.org/10.1017/9781139016476.
Peng, S., Piao, S., Ciais, P., Friedlingstein, P., Ottle, C., Bréon, F.-M., Nan, H., Zhou, L., Myneni, R.B., 2012. Surface urban heat island across 419 global big cities. Environ. Sci. Technol. 46, 696–703. https://doi.org/10.1021/es2030438.
Rothfusz, L.P., Headquarters, N.S.R., 1990. The heat index equation. In: more than you ever wanted to know about heat index), 9023. National Oceanic and Atmospheric Administration, National Weather Service, Office of Meteorology, Fort Worth, Texas, p. 640.
Shandas, V., Voelkel, J., Williams, J., Hoffman, J., 2019. Integrating satellite and ground measurements for predicting locations of extreme urban heat. Climate 7. https://doi.org/10.3390/cli7010005.
Stewart, I.D., Oke, T.R., 2012. Local climate zones for urban temperature studies. Bull. Am. Meteorol. Soc. 93, 1879–1900. https://doi.org/10.1175/BAMS-D-11-00019.1.
Sun, T., Grimmond, S., 2019. A Python-enhanced urban land surface model SuPy (SUEWS in Python, v2019.2): development, deployment and demonstration. Geosci. Model Dev. 12, 2781–2795. https://doi.org/10.5194/gmd-12-2781-2019.
Tang, Y., Sun, T., Luo, Z., Omidvar, H., Theeuwes, N., Xie, X., Xiong, J., Yao, R., Grimmond, S., 2021. Urban meteorological forcing data for building energy simulations. Build. Environ. 204 https://doi.org/10.1016/j.buildenv.2021.108088.
US Census Bureau, 2022. Quick Facts-Austin, Texas.
Voogt, J.A., Oke, T.R., 1997. Complete Urban Surface Temperatures. J. Appl. Meteorol. 36, 1117–1132. https://doi.org/10.1175/1520-0450(1997)036<1117:CUST>2.0.CO;2.
Voogt, J.A., Oke, T.R., 2003. Thermal remote sensing of urban climates. Remote Sens. Environ. 86, 370–384. https://doi.org/10.1016/S0034-4257(03)00079-8.
Ward, H.C., Kotthaus, S., Järvi, L., Grimmond, C.S.B., 2016. Surface urban energy and water balance scheme (SUEWS): development and evaluation at two UK sites. Urban Clim. 18, 1–32. https://doi.org/10.1016/j.uclim.2016.05.001.